Simultaneous control of the Dzyaloshinskii-Moriya interaction and magnetic anisotropy in nanomagnetic trilayers

A. L. Balk,[1,2,3] K-W. Kim,[1,2] D. T. Pierce,[1] M. D. Stiles,[1] J. Unguris,[1] and S. M. Stavis[1,*]
[1]Center for Nanoscale Science and Technology, National Institute of Standards and Technology, Gaithersburg, Maryland 20899 USA
[2]Maryland NanoCenter, University of Maryland, College Park, Maryland 20742 USA
[3]National High Magnetic Field Laboratory, Los Alamos National Laboratory, Los Alamos, New Mexico 87545 USA
(Received 3 October 2016; revised manuscript received 27 March 2017; published 17 August 2017)

Magneto-optical Kerr effect (MOKE) microscopy measurements of magnetic bubble domains demonstrate that Ar^+ irradiation around 100 eV can tune the Dzyaloshinskii-Moriya interaction (DMI) in Pt/Co/Pt trilayers. Varying the irradiation energy and dose changes the DMI sign and magnitude separately from the magnetic anisotropy, allowing tuning of the DMI while holding the coercive field constant. This simultaneous control emphasizes the different physical origins of these effects. To accurately measure the DMI, we propose and apply a physical model for a poorly understood peak in domain wall velocity at zero in-plane field. The ability to tune the DMI with the spatial resolution of the Ar^+ irradiation enables new fundamental investigations and technological applications of chiral nanomagnetics.

DOI: 10.1103/PhysRevLett.119.077205

The Dzyaloshinskii-Moriya interaction (DMI) is a chiral energy term leading to interesting nanoscale magnetic phenomena [1–4]. Examples include Skyrmions [5–10], domain wall motion [11–15], helical spin textures [16,17], and spin-orbit torque magnetization switching [18–20]. However, such phenomena depend on a combination of the DMI and nonchiral magnetic effects such as anisotropy [21–23], Zeeman energy [4,24,25], and dipolar interaction [26–28]. While previous studies have demonstrated several methods for controlling the DMI [29–32], these also lead to variations in magnetic anisotropy and exchange interaction, making it difficult to reach a specific location in the phase space of micromagnetic energy parameters. Furthermore, these methods cannot be applied to different regions of the same sample, requiring separate samples to vary the DMI. Addressing these limitations, we demonstrate postgrowth Ar^+ irradiation around 100 eV as a method to tune the sign and magnitude of the DMI, separately from the coercive field $\mu_0 H_c$, in a single trilayer of Pt/Co/Pt, a model nanomagnetic system with perpendicular interfacial anisotropy.

First, we report the sample growth and Ar^+ irradiation procedures that we use to tune the properties of the trilayer. Then, we describe the magneto-optical Kerr effect (MOKE) microscopy technique that we use to measure domain wall motion and infer the effective DMI field $\mu_0 H_{\mathrm{DMI}}$ in the trilayer. Some of our data sets show a previously observed but unexplained peak in domain wall velocity at zero in-plane field, for which we propose a physical model. We fit our data with this model and demonstrate that we can simultaneously control $\mu_0 H_{\mathrm{DMI}}$ and $\mu_0 H_c$ by varying the energy and dose of Ar^+ irradiation, enabling us to implement arbitrary combinations of these magnetic parameters. Last, we attribute the separate tuning of $\mu_0 H_{\mathrm{DMI}}$ and $\mu_0 H_c$ [33–36] to the distinct effects of etching the top Pt layer and modifying the disorder of the Co/Pt interfaces by Ar^+ irradiation.

We study a single trilayer of Pt(35 nm)/Co(0.8 nm)/Pt(1.7 nm) that we sputter on a p-type silicon wafer (Supplemental Material S1 [37]). We use a shadow mask to irradiate the trilayer with a spatially varying dose of Ar^+ at a range of energies $E_{\mathrm{Ar+}}$ from 50 eV to 140 eV in increments of 5 eV, and then remove the sample from vacuum for measurement in air. The irradiation reduces the as-grown value of $\mu_0 H_c \approx 80$ mT to values ranging to 0 mT where spontaneous domain fluctuations [38] and a spin reorientation transition [35] occur. For this trilayer and these energies, the spin reorientation transition occurs with Ar^+ doses of approximately 2×10^{15} cm^{-2} to 2×10^{16} cm^{-2}.

We measure the DMI of different regions of this trilayer using MOKE microscopy of the expansion of magnetic bubble domains with applied out-of-plane and in-plane fields B_z and B_y. In this technique, B_z creates and expands bubbles while the DMI and B_y lead to asymmetry of this expansion [Fig. 1(a)] by modifying the energy of the Néel walls surrounding the bubbles [29,39,40]. For example, the left side of the left bubble in Fig. 1(a) expands faster in the direction of B_y because this Néel wall has a lower energy due to B_y, corresponding to $\mu_0 H_{\mathrm{DMI}} > 0$ mT. Building on the earlier reports, we pulse B_z to generate and annihilate magnetic bubbles at a repetition frequency of 50 Hz to 150 Hz, which is higher than the imaging frequency of 10 Hz. Therefore, each MOKE micrograph [Figs. 1(b) and 1(c)] shows a bubble at its maximum size, from the average of 5 to 15 expansions. While applying pulses of B_z, we apply B_y as a triangle wave with a frequency of 50 mHz, which is much slower than the B_z repetition frequency.

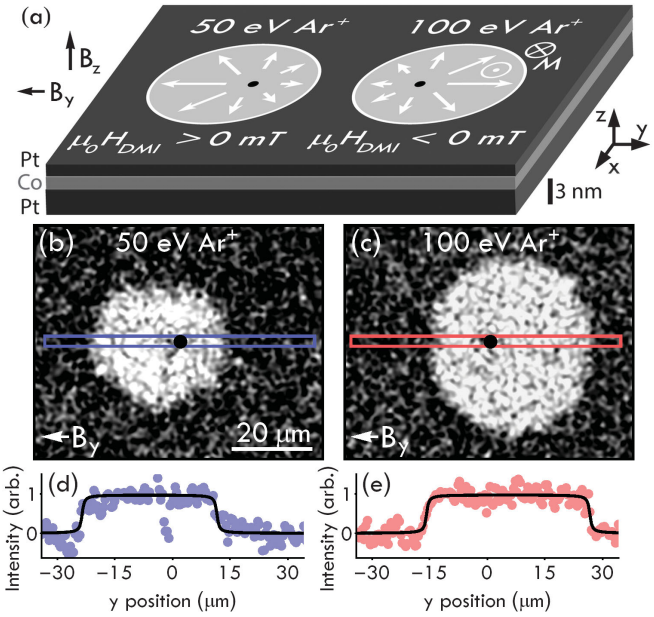

FIG. 1. Ar^+ irradiation of a Pt/Co/Pt trilayer controls the sign of the Dzyaloshinskii-Moriya interaction (DMI). (a) A simplified schematic shows magnetic bubble domains with positive M_z (light gray circles) in trilayer regions irradiated with 50 eV Ar^+ or 100 eV Ar^+, expanding asymmetrically (white arrows) in opposite y directions from nucleation sites (black dots) in response to applied fields B_z and B_y. The direction of this asymmetric expansion indicates the sign of $\mu_0 H_{\mathrm{DMI}}$. (b),(c) Magneto-optical Kerr effect (MOKE) micrographs showing corresponding experimental results. We have spatially filtered and removed backgrounds from these representative micrographs for clarity. The Ar^+ dose is approximately 2×10^{16} cm^{-2} for (b) and approximately 2×10^{15} cm^{-2} for (c). Black dots indicate the approximate position of bubble nucleation. Blue and red rectangles indicate regions from which we take profiles to determine domain wall displacements. (d),(e) Blue and red markers are profiles from boxed regions in (b) and (c) averaged across the x direction. Black curves are arctangent fits to extract domain wall displacements with standard uncertainties of approximately 400 nm.

Therefore, the bubbles that we measure accurately reflect how B_y affects their expansion. Supplemental Material S2 [37] presents details of the field excitation technique. To measure domain wall displacements in real time, we take a cross-sectional strip of each bubble [Figs. 1(b) and 1(c), blue and red rectangles], average these strips across the x direction, [Figs. 1(d) and 1(e), blue and red markers], and fit each resulting profile to arctangent functions [Figs. 1(d) and 1(e), black lines] which empirically model the optically broadened profile of the domain walls (Supplemental Material S3 [37]) and superresolve their positions. We divide the domain wall displacements by the duration of the B_z pulses to obtain the mean velocity v of each domain wall during bubble expansion.

To perform a measurement of the DMI, we measure v as a function of B_y. The domain wall comprising the bubble has opposite symmetry on either side of the bubble with respect to B_y, so that in the reference frame of the domain wall the effective magnetic field $B_{y(\mathrm{eff})}$ is opposite in sign for each side of the bubble. (Fig. 2, inset). Therefore, we resample the raw data, which includes multiple cycles of B_y, by averaging data points with $B_{y(\mathrm{eff})}$ within 1 mT of each other (Fig. 2). These curves come from a region of the trilayer that we expose to 125 eV Ar^+, with $\mu_0 H_c \approx 3$ mT, and is an average of 12 B_y cycles. The similar behavior of the domain wall on both sides of the bubble indicates the preservation of the domain wall chirality around the bubble, which is typical for all bubbles in this study. The data does not show evidence for chiral damping [41], as it does not have a significant asymmetry about its minimum value (Supplemental Material S4 [37]).

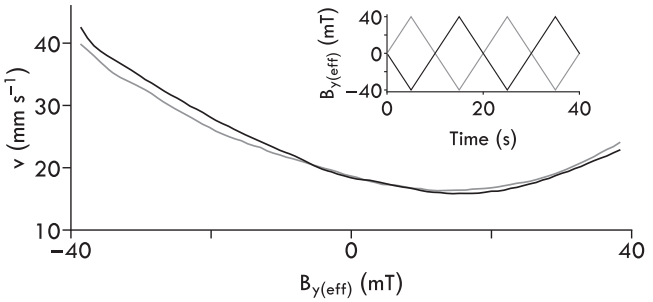

FIG. 2. Representative data shows a simultaneous measurement of the velocity v of a domain wall on the positive y (gray) and negative y (black) sides of a bubble. The domain wall moves similarly on both sides of the bubble in response to the effective magnetic field $B_{y(\mathrm{eff})}$, with a reversed sign for opposite sides. We attribute the small difference between the curves to a misalignment of B_y which adds a z component to the total field. Standard uncertainties of v are approximately 0.2 mm s^{-1}. Inset: simulated data sets show that $B_{y(\mathrm{eff})}$ is opposite in sign for the domain wall on each side of the bubble, due to the opposite spatial symmetry.

For a systematic study of the DMI, we obtain over 400 v curves such as those in Fig. 2, although averaging over only two cycles of B_y. To compare the results from many bubbles which may not have the same v, we normalize each curve to its value at $B_{y(\mathrm{eff})} = 0$, $v_{\mathrm{norm}} = v/v_{B_{y(\mathrm{eff})}=0}$. Additionally, we measure the mean v_{norm} of the domain wall on either side of the bubble, since it behaves similarly with response to $B_{y(\mathrm{eff})}$ (Fig. 2). Typical standard uncertainties of v_{norm} after such averaging are about 0.01. Finally, after each bubble measurement, we determine the local $\mu_0 H_c$ of the trilayer by measuring a hysteresis loop at the location of the bubble with a B_z ramp rate of approximately 20 mT s^{-1}. Figure 3 shows a selection of the v_{norm} curves (gray markers), arranged by $E_{\mathrm{Ar}+}$ and $\mu_0 H_c$. We determine $\mu_0 H_{\mathrm{DMI}}$ as the negative of the in-plane field which minimizes the quadratic component of v_{norm}, defining positive $\mu_0 H_{\mathrm{DMI}}$ as acting perpendicular to the surface of the domain wall, in the direction pointing from an $M_z > 0$ region to an $M_z < 0$ region [39,42]. This definition is consistent with positive $\mu_0 H_{\mathrm{DMI}}$ leading to right-hand

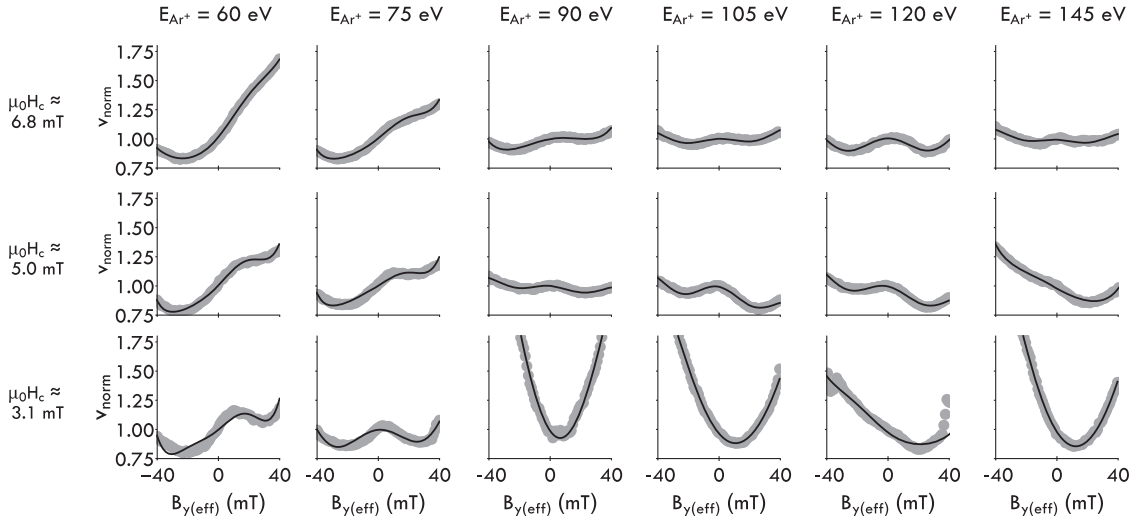

FIG. 3 Representative curves show the normalized domain wall velocity v_{norm} (gray markers) at six values of $E_{\mathrm{Ar+}}$ for doses that give three values of $\mu_0 H_c$. Black curves are the fits to extract the value of K_{pin} and $\mu_0 H_{\mathrm{DMI}}$. The data sets at $\mu_0 H_c \approx 5.0$ mT exemplify bipolar tuning of $\mu_0 H_{\mathrm{DMI}}$ at constant $\mu_0 H_c$. Standard uncertainties of v_{norm} are typically 0.01, which is smaller than the data markers in most cases.

domain walls, and the DMI energy $E_{\mathrm{DMI}} = -\mathbf{D} \cdot (\mathbf{S}_1 \times \mathbf{S}_2)$, with $\mathbf{S}_1$ and $\mathbf{S}_2$ representing the state of adjacent spins, and $\mathbf{D}$ the DMI vector. In Fig. 3, the $\mu_0 H_c \approx 5.0$ mT row exemplifies tuning of $\mu_0 H_{\mathrm{DMI}}$ by $E_{\mathrm{Ar+}}$.

Many of the curves show a peak in v_{norm} for $B_{y(\mathrm{eff})} \approx 0$, for example, in the $\mu_0 H_c \approx 3.1$ mT, $E_{\mathrm{Ar+}} = 75$ eV curve, which prevents fitting this data to a simple quadratic function to accurately extract $\mu_0 H_{\mathrm{DMI}}$. Previous studies have also reported this peak [31,41–43], ruling out experimental artifacts specific to our experiment.

We propose a physical model as a possible explanation for the peak—a B_y-dependent perturbation to the prefactor v_0 in the domain wall creep equation, $v = v_0 \exp(-\kappa {B_z}^{-1/4})$. In this equation, κ is a quantity related to the domain wall surface tension, pinning potential, and temperature. In most cases [39,44,45], changes in κ dominate changes in domain wall velocity, but if the exponent is small or κ is insensitive to small values of B_y, then changes in v_0 may dominate [41]. We believe that this is the case here, as the peak amplitude scales differently from the overall parabolic behavior of v in response to a changing B_z (not shown). The value of v_0 depends on the attempt frequency ω of the domain walls in the pinning potential E_{pin} [46,47]. ω is proportional to the square root of the curvature $d^2 E_{\mathrm{pin}}/d\theta^2$ of the pinning potential. A field such as B_y changes the curvature by moving the configuration of the domain wall away from the minimum of E_{pin}. Since the minimum of E_{pin} corresponds to a maximum of $d^2 E_{\mathrm{pin}}/d\theta^2$ for most pinning potentials [41], it also corresponds to a maximum in ω. Therefore, any deviation of the minimum energy configuration of the domain wall from its value at $B_y = 0$ will decrease ω and thus v_0, in an amount proportional to the square root of $d^2 E_{\mathrm{pin}}/d\theta^2$. This explanation predicts a peak in v_{norm} at $B_y = 0$, as is evident if we model the pinning potential by an anisotropy energy minimum with equilibrium angle θ_{eq} that varies around 0 as the field B_y varies:

$$v_0 \propto \omega \propto \sqrt{\left.\frac{d^2 E_{\mathrm{anis}}}{d\theta^2}\right|_{\theta=\theta_{\mathrm{eq}}}} = \sqrt{2K_{\mathrm{pin}} \cos(2\theta_{\mathrm{eq}})}$$
$$= \sqrt{2K_{\mathrm{pin}} \cos\left(\frac{2MB_y}{2K_{\mathrm{pin}} + MB_z}\right)}. \quad (1)$$

In this model, $M = 5 \times 10^5$ Am^{-1} is an estimate of the saturation magnetization, which we obtain from a previous study [48], and K_{pin} is the effective anisotropy constant for pinning. Since v_0 is outside the exponent in the creep law which predicts domain wall motion, this modification manifests as a multiplicative correction to the domain wall creep law, which is approximately quadratic in B_y at low fields [39]. Therefore, using the method of damped least squares, we fit (Fig. 3, black lines) the v_{norm} curves to the product of a quadratic function which approximates the domain wall creep law with the DMI, and an approximation of relation (1) at $\theta_{\mathrm{eq}} \approx 0$ (Supplemental Material S5 [37]). This relation fits most of the features in the experimental data, and extracts values of K_{pin} and $\mu_0 H_{\mathrm{DMI}}$ that are robust to the details of the fit.

Using this model, we extract a value of $K_{\mathrm{pin}} = 6$ kJ m$^{-3} \pm 2$ kJ m^{-3}, denoting the mean and standard deviation of 100 v_{norm} curves that show an appreciable central peak. This value is much smaller than typically measured values [44] of the uniaxial anisotropy constant K_1, but we can reconcile this discrepancy by noting that the pinning potential should be more complicated than a simple

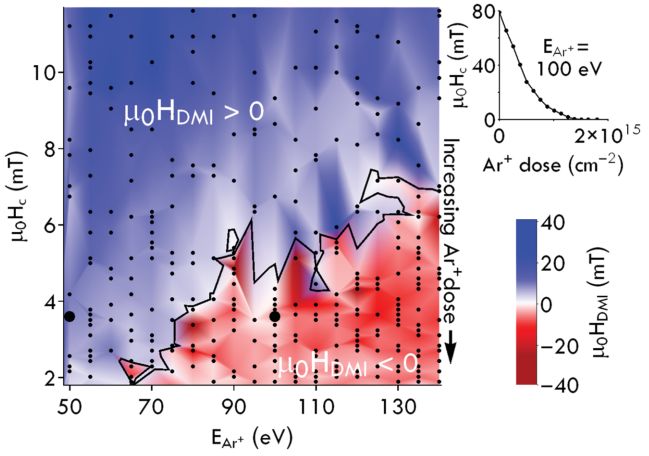

FIG. 4. A surface plot of $\mu_0 H_{\mathrm{DMI}}$ shows systematic variation as a function of $\mu_0 H_c$ and $E_{\mathrm{Ar+}}$. Ar^+ dose increases toward the bottom of this surface plot. The black contour indicates the boundary between positive (blue) and negative (red) $\mu_0 H_{\mathrm{DMI}}$. Circular black markers indicate the $\mu_0 H_c$ and $E_{\mathrm{Ar+}}$ values of the measurements between which the color map interpolates. The two large black markers indicate the approximate parameters corresponding to Supplemental Material Video S8 [37]. Inset: $\mu_0 H_c$ decreases monotonically with Ar^+ dose for a sample with $E_{\mathrm{Ar+}} = 100$ eV.

uniaxial anisotropy. We do observe a correlation between K_{pin} and $\mu_0 H_c$ (Supplemental Material S6 [37]), supporting our model of the peak in v_{norm} as an effective anisotropy.

The values of $\mu_0 H_{\mathrm{DMI}}$ that we extract show systematic variation as a function of $\mu_0 H_c$ and $E_{\mathrm{Ar+}}$ (Fig. 4, surface plot), which is the main result of our study–simultaneous control of $\mu_0 H_{\mathrm{DMI}}$ and $\mu_0 H_c$. The color scale in Fig. 4 is a linear interpolation between the $\mu_0 H_{\mathrm{DMI}}$ values obtained at the $\mu_0 H_c$ and $E_{\mathrm{Ar+}}$ conditions that the small black markers indicate. Regions of positive $\mu_0 H_{\mathrm{DMI}}$ (blue) and negative $\mu_0 H_{\mathrm{DMI}}$ (red) are visible, as is the contour separating them (black line). The values of $\mu_0 H_{\mathrm{DMI}}$ have typical standard uncertainties of 1 mT. However, the scatter of the data, manifesting for example as irregularity of the black contour line, indicates that variation in $\mu_0 H_{\mathrm{DMI}}$ due to heterogeneity of the trilayer exceeds measurement uncertainty. We also confirm that Ar^+ dose monotonically controls $\mu_0 H_c$ by measuring $\mu_0 H_c$ as a function of Ar^+ dose for $E_{\mathrm{Ar+}} = 100$ eV (Fig. 4, inset). Supplemental Material Fig. S7 [37] shows data over the full range of $\mu_0 H_c$ and presents uncertainty evaluation.

To demonstrate spatial resolution of this tuning, we prepare two nearby regions of the trilayer to have the same $\mu_0 H_c$ of 3.6 mT, but different values of $\mu_0 H_{\mathrm{DMI}}$, 20 mT and −20 mT, with exposure to 50 eV Ar^+ and 100 eV Ar^+, respectively (large black markers, Fig. 4). These regions are close enough such that the effects of positive and negative $\mu_0 H_{\mathrm{DMI}}$ are evident with identical B_y and B_z excitation, in the same field of view of the MOKE microscope (Supplemental Material Video S8 [37]).

While both $\mu_0 H_{\mathrm{DMI}}$ and $\mu_0 H_c$ depend on spin-orbit coupling at the Pt/Co interfaces, our results indicate that they depend differently on the details of the layers and interfaces. A stopping and range of ions in matter (SRIM) simulation [49] (Supplementary Material S9 [37]) shows that around $E_{\mathrm{Ar+}} = 100$ eV, Ar^+ primarily influences the top Pt and Co layers. Auger spectroscopy (Supplementary Material S9 [37]) does not show evidence of Ar implantation, and indicates that the change of the sign of $\mu_0 H_{\mathrm{DMI}}$ is associated with removal of the top Pt monolayer. Although the different behavior of $\mu_0 H_{\mathrm{DMI}}$ and $\mu_0 H_c$ with $E_{\mathrm{Ar+}}$ and Ar^+ dose may be complicated, previous studies provide some guidance. Several studies [33–36] have shown that ion-induced interfacial disorder, and reduction of the thickness of the top Pt layer [50], decrease $\mu_0 H_c$, while $\mu_0 H_{\mathrm{DMI}}$ is primarily sensitive to the interfacial Pt monolayers [51]. Therefore, removal of the top Pt could affect $\mu_0 H_{\mathrm{DMI}}$ in two ways, eliminating the positive influence of the layer on $\mu_0 H_{\mathrm{DMI}}$ [52], and allowing oxidation of the Co [53,54].

Eliminating the influence of the top Pt should have a strong influence on $\mu_0 H_{\mathrm{DMI}}$. The etch rate of Pt vanishes at lower $E_{\mathrm{Ar+}}$ [55], and depends differently on $E_{\mathrm{Ar+}}$ than interfacial disorder does. This suggests that, for a given thickness of etched Pt, higher energy Ar^+ causes less interfacial disorder than lower energy Ar^+, causing an $E_{\mathrm{Ar+}}$ dependence of $\mu_0 H_{\mathrm{DMI}}$ at fixed $\mu_0 H_c$. For example, exposure to 130 eV Ar^+ leads to a large negative $\mu_0 H_{\mathrm{DMI}}$ after removal of the top Pt layer, but 50 eV Ar^+ causes enough disorder to drive the film to the spin reorientation transition at doses necessary to remove the top Pt layer.

To test the effect of Co oxidation on $\mu_0 H_{\mathrm{DMI}}$, we deposit a layer of Au with a thickness of approximately 10 nm immediately after Ar^+ irradiation in vacuum. After exposure to air, we measure similar values of $\mu_0 H_{\mathrm{DMI}}$ with and without the Au layer (Supplementary Material S10 [37]). This suggests that Pt removal is the primary mechanism for our simultaneous control, but does not rule out oxidation as a factor, as we are not certain that the Au layer is hermetic, and we do not know of any influence of the Au itself on $\mu_0 H_{\mathrm{DMI}}$. Measurements in vacuum could elucidate these effects.

In conclusion, we have demonstrated the use of Ar^+ irradiation around 100 eV to tune the sign and magnitude of the DMI in ultrathin Pt/Co/Pt trilayers. The tuning is spatially variable, separately from $\mu_0 H_c$. At low values of the DMI, we observe a peak in domain wall velocity which we propose to explain by a modification of the depinning attempt frequency in the creep regime of domain wall motion. This model may also explain a discrepancy between measurements of $\mu_0 H_{\mathrm{DMI}}$ by domain wall motion and Brillouin light scattering [42], which do not account for the influence of the peak in domain wall velocity. Our technique for simultaneous control of $\mu_0 H_{\mathrm{DMI}}$ and $\mu_0 H_c$ on a single chip enables systematic study of the effects of the DMI in isolation from stronger interactions [56], and potentially allows micro- and nanopatterning of the

DMI [57]. Finally, this new level of control will enable magnetic materials with engineered DMI for proposed and existing technological applications [58–60].

The authors acknowledge Edward Cazalas for performing and interpreting SRIM simulations, Kerry Siebein for assistance with x-ray diffraction measurements, and Carl Boone, Paul Haney, Daniel Gopman, and J. Alexander Liddle for thoughtful reviews and helpful criticism. K. W. K acknowledges Hyun-Woo Lee for fruitful discussion. A. L. B. and K. W. K. acknowledge support of this research under the Cooperative Research Agreement between the University of Maryland and the National Institute of Standards and Technology Center for Nanoscale Science and Technology, Award No. 70NANB10H193, through the University of Maryland. K. W. K also acknowledges support by Basic Science Research Program through the National Research Foundation of Korea (NRF) funded by the Ministry of Education (2016R1A6A3A03008831).

*Corresponding author.
sstavis@nist.gov

[1] T. Moriya, Phys. Rev. **120**, 91 (1960).
[2] M. Heide, G. Bihlmayer, and S. Blügel, Phys. Rev. B **78**, 140403 (2008).
[3] G. Chen *et al.*, Phys. Rev. Lett. **110**, 177204 (2013).
[4] X. Z. Yu, Y. Onose, N. Kanazawa, J. H. Park, J. H. Han, Y. Matsui, N. Nagaosa, and Y. Tokura, Nature (London) **465**, 901 (2010).
[5] T. Schwarze, J. Waizner, M. Garst, A. Bauer, I. Stasinopoulos, H. Berger, C. Pfleiderer, and D. Grundler, Nat. Mater. **14**, 478 (2015).
[6] X. Yu, A. Kikkawa, D. Morikawa, K. Shibata, Y. Tokunaga, Y. Taguchi, and Y. Tokura, Phys. Rev. B **91**, 054411 (2015).
[7] W. Jiang *et al.*, Nat. Phys.. **13**, 162 (2017).
[8] S. Woo *et al.*, Nat. Mater. **15**, 501 (2016).
[9] A. Fert, V. Cros, and J. Sampaio, Nat. Nanotechnol. **8**, 152 (2013).
[10] W. Jiang *et al.*, Science **349**, 283 (2015).
[11] A. Thiaville, S. Rohart, É. Jué, V. Cros, and A. Fert, Europhys. Lett. **100**, 57002 (2012).
[12] E. Martinez, S. Emori, and G. S. D. Beach, Appl. Phys. Lett. **103**, 072406 (2013).
[13] K. Ueda *et al.*, Appl. Phys. Express **7**, 053006 (2014).
[14] Y. Yoshimura *et al.*, Nat. Phys. **12**, 157 (2016).
[15] S. Emori, U. Bauer, S.-M. Ahn, E. Martinez, and G. S. Beach, Nat. Mater. **12**, 611 (2013).
[16] P. Bak and M. H. Jensen, J. Phys. C **13**, L881 (1980).
[17] K. Bu, H. Kwon, S. Kang, H. Kim, and C. Won, J. Magn. Magn. Mater. **343**, 32 (2013).
[18] N. Perez, E. Martinez, L. Torres, S. H. Woo, S. Emori, and G. S. D. Beach, Appl. Phys. Lett. **104**, 092403 (2014).
[19] O. J. Lee, L. Q. Liu, C. F. Pai, Y. Li, H. W. Tseng, P. G. Gowtham, J. P. Park, D. C. Ralph, and R. A. Buhrman, Phys. Rev. B **89**, 024418 (2014).
[20] A. W. Rushforth, Appl. Phys. Lett. **104**, 162408 (2014).
[21] H. Kwon, K. Bu, Y. Wu, and C. Won, J. Magn. Magn. Mater. **324**, 2171 (2012).
[22] C.-F. Pai, M. Mann, A. J. Tan, and G. S. D. Beach, Phys. Rev. B **93**, 144409 (2016).
[23] T. Michael and S. Trimper, Phys. Rev. B **82**, 052401 (2010).
[24] S. Mühlbauer, B. Binz, F. Jonietz, C. Pfleiderer, A. Rosch, A. Neubauer, R. Georgii, and P. Böni, Science **323**, 915 (2009).
[25] O. Boulle, S. Rohart, L. D. Buda-Prejbeanu, E. Jué, I. M. Miron, S. Pizzini, J. Vogel, G. Gaudin, and A. Thiaville, Phys. Rev. Lett. **111**, 217203 (2013).
[26] G. Chen, T. Ma, A. T. N'Diaye, H. Kwon, C. Won, Y. Wu, and A. K. Schmid, Nat. Commun. **4**, 2671 (2013).
[27] N. Samarth and J. Furdyna, Solid State Commun. **65**, 801 (1988).
[28] J.-V. Kim, R. L. Stamps, and R. E. Camley, Phys. Rev. Lett. **117**, 197204 (2016).
[29] A. Hrabec, N. A. Porter, A. Wells, M. J. Benitez, G. Burnell, S. McVitie, D. McGrouther, T. A. Moore, and C. H. Marrows, Phys. Rev. B **90**, 020402 (2014).
[30] R. A. Khan, P. M. Shepley, A. Hrabec, A. W. J. Wells, B. Ocker, C. H. Marrows, and T. A. Moore, Appl. Phys. Lett. **109**, 132404 (2016).
[31] R. Lavrijsen, D. Hartmann, A. van den Brink, Y. Yin, B. Barcones, R. Duine, M. Verheijen, H. Swagten, and B. Koopmans, Phys. Rev. B **91**, 104414 (2015).
[32] A. W. J. Wells, P. M. Shepley, C. H. Marrows, and T. A. Moore, Phys. Rev. B **95**, 054428 (2017).
[33] C. Chappert *et al.*, Science **280**, 1919 (1998).
[34] H. Bernas *et al.*, Nucl. Instrum. Methods Phys. Res., Sect. B **148**, 872 (1999).
[35] N. Bergeard, J. P. Jamet, J. Ferré, A. Mougin, and J. Fassbender, J. Appl. Phys. **108**, 103915 (2010).
[36] J. Fassbender and J. McCord, J. Magn. Magn. Mater. **320**, 579 (2008).
[37] See Supplemental Material at http://link.aps.org/supplemental/10.1103/PhysRevLett.119.077205 for details of sample preparation, field excitation, data reduction, model derivation, video data, Auger spectroscopy, SRIM simulations, and control measurements.
[38] A. L. Balk, M. D. Stiles, and J. Unguris, Phys. Rev. B **90**, 184404 (2014).
[39] S.-G. Je, D.-H. Kim, S.-C. Yoo, B.-C. Min, K.-J. Lee, and S.-B. Choe, Phys. Rev. B **88**, 214401 (2013).
[40] D.-Y. Kim, D.-H. Kim, J. Moon, and S.-B. Choe, Appl. Phys. Lett. **106**, 262403 (2015).
[41] E. Jué *et al.*, Nat. Mater. **15**, 272 (2016).
[42] R. Soucaille *et al.*, Phys. Rev. B **94**, 104431 (2016).
[43] Y. Kabanov, Y. Iunin, V. Nikitenko, A. Shapiro, R. Shull, L. Zhu, and C. Chien, IEEE Trans. Magn. **46**, 2220 (2010).
[44] P. J. Metaxas, J. P. Jamet, A. Mougin, M. Cormier, J. Ferré, V. Baltz, B. Rodmacq, B. Dieny, and R. L. Stamps, Phys. Rev. Lett. **99**, 217208 (2007).
[45] S. Lemerle, J. Ferré, C. Chappert, V. Mathet, T. Giamarchi, and P. Le Doussal, Phys. Rev. Lett. **80**, 849 (1998).
[46] J. Gorchon, S. Bustingorry, J. Ferré, V. Jeudy, A. B. Kolton, and T. Giamarchi, Phys. Rev. Lett. **113**, 027205 (2014).
[47] J. Schratzberger, J. Lee, M. Fuger, J. Fidler, G. Fiedler, T. Schrefl, and D. Suess, J. Appl. Phys. **108**, 033915 (2010).
[48] W. Zeper, F. Greidanus, P. Carcia, and C. Fincher, J. Appl. Phys. **65**, 4971 (1989).

[49] J. F. Ziegler, M. D. Ziegler, and J. P. Biersack, Nucl. Instrum. Methods Phys. Res., Sect. B **268**, 1818 (2010).
[50] Z. Zhang, P. E. Wigen, and S. S. P. Parkin, J. Appl. Phys. **69**, 5649 (1991).
[51] H. Yang, A. Thiaville, S. Rohart, A. Fert, and M. Chshiev, Phys. Rev. Lett. **115**, 267210 (2015).
[52] M. Quinsat, Y. Ootera, T. Shimada, M. Kado, S. Hashimoto, H. Morise, S. Nakamura, and T. Kondo, AIP Adv. **7**, 056318 (2017).
[53] A. Belabbes, G. Bihlmayer, S. Blügel, and A. Manchon, Sci. Rep. **6**, 24634 (2016).
[54] H. Yang, O. Boulle, V. Cros, A. Fert, and M. Chshiev, arXiv:1603.01847.
[55] Y. Yamamura and H. Tawara, At. Data Nucl. Data Tables **62**, 149 (1996).
[56] K. M. D. Hals and A. Brataas, Phys. Rev. B **89**, 064426 (2014).
[57] J. Mulkers, B. Van Waeyenberge, and M. V. Milošević, Phys. Rev. B **95**, 144401 (2017).
[58] O. Heinonen, W. Jiang, H. Somaily, S. G. E. te Velthuis, and A. Hoffmann, Phys. Rev. B **93**, 094407 (2016).
[59] A. L. Balk, C. Hangarter, S. M. Stavis, and J. Unguris, Appl. Phys. Lett. **106**, 112402 (2015).
[60] D. A. Gilbert, B. B. Maranville, A. L. Balk, B. J. Kirby, P. Fischer, D. T. Pierce, J. Unguris, J. A. Borchers, and K. Liu, Nat. Commun. **6**, 8462 (2015).